



An experimental analysis of the correlation between electronic structure and room temperature magnetism in Cu-doped CoFe_2O_4 spinel ferrite

M. Thavarani¹ · M. Charles Robert² · N. Pavithra¹ · S. Balaji Prasath² · Y. B. Kannan³ · A. Ansar Ahamed²

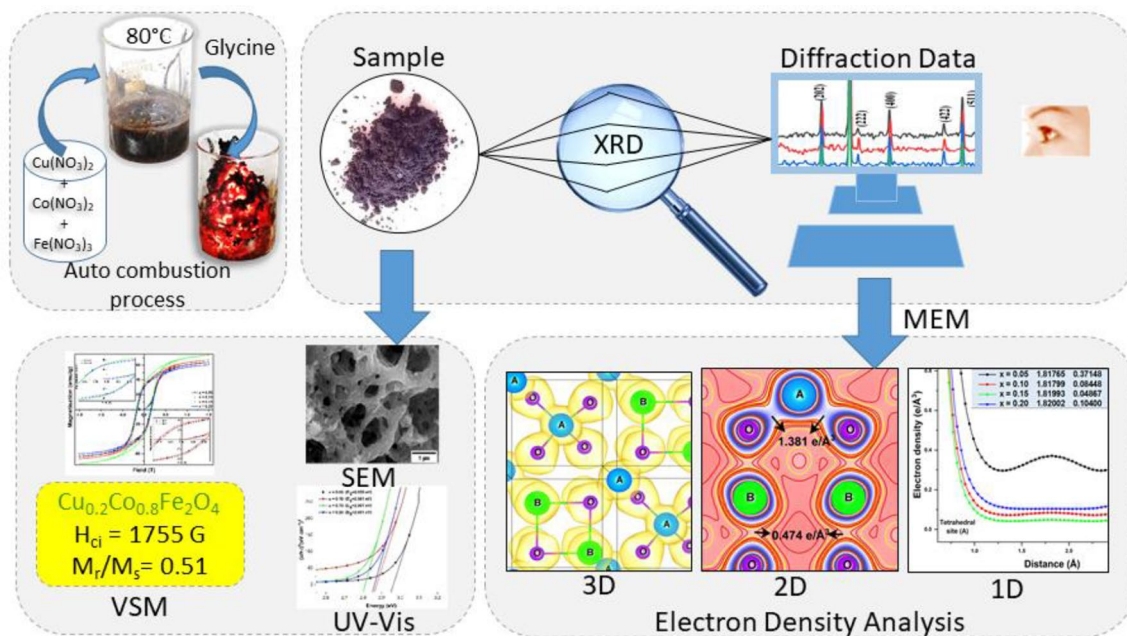
Received: 21 April 2022 / Accepted: 23 June 2022

© The Author(s), under exclusive licence to Springer-Verlag GmbH, DE part of Springer Nature 2022

Abstract

Cu-doped CoFe_2O_4 spinel ferrites with composition $\text{Cu}_x\text{Co}_{1-x}\text{Fe}_2\text{O}_4$: $x=0.05, 0.1, 0.15, 0.2$ have been synthesized by sol-gel self-combustion method. Cation distribution using XRD data by intensity ratio and Rietveld method revealed perfect inverse spinel structure, further confirmed with Vibration Sample Magnetometer (VSM) results explaining two sub-lattice collinear models. The room temperature VSM analysis reveals ferromagnetism in all compositions of the samples with a maximum saturation value of 73.587 emu/g at 1.5 T for the composition $x=0.15$ and maximum coercivity 1754.67 G and squareness ratio 51% for the composition $x=0.2$. The above result may be the highest value of coercivity and squareness ratio reported at room temperature for Cu-doped CoFe_2O_4 spinel ferrites. The electron density distribution using XRD data utilizing Maximum Entropy Method (MEM) visualizes the electronic structure. All compositions show strong tetrahedral A–O covalent bonding with Oxygen ions. Moderate covalent octahedral B–O ionic bonding for the compositions $x=0.05, 0.1$ and 0.15 and ionic bonding for the composition $x=0.2$ are observed. The composition $\text{Cu}_{0.2}\text{Co}_{0.8}\text{Fe}_2\text{O}_4$ with the maximum tetrahedral covalent and octahedral ionic bonding has the highest observed magnetic parameters.

Graphical abstract



Extended author information available on the last page of the article

Keywords Ferromagnetism in spinel ferrite · Squareness ratio · MEM · Electron density analysis · Cation distribution · VSM

1 Introduction

Cubic spinel ferrites are magnetic materials with an extensive range of magnetic properties like saturation magnetization, remanent magnetization, and coercivity for various industrial, medical, biological and scientific applications [1–4]. Generally, spinel ferrites' physical and chemical properties can be tuned to desired applications based on the type of metal cations, their composition, and the distribution in the crystal structure [5]. Cobalt ferrite is a hard material with high coercivity, high anisotropy, high saturation magnetization, and its physical hardness and chemical stability [6], makes Cobalt ferrite a useful material for various applications like magnetic recording, microwave and radar devices, ferrofluids and magnetic cooling [7]. Cobalt spinel ferrite has an inverse spinel structure with the occupation of Co^{2+} ions in the octahedral B site, and Fe^{3+} in both tetrahedral A and octahedral B sites [8]. Cobalt ferrite was successfully synthesized by different methods such as chemical co-precipitation method, sol–gel, solvothermal, reverse micelles, sonication, green synthesis and auto-combustion method. Though there are many methods to synthesize Cobalt ferrite, one-step self-combustion method is a cost-effective, simple and high yield method for synthesizing bulk cobalt spinel ferrites [9–15]. Some of the works reported in the literature on both undoped and Cu-doped CoFe_2O_4 are available.

Hydrothermal synthesis of CoFe_2O_4 with and without ball milling was reported to have a maximum coercivity of 1.9 kOe and 4.1 kOe and magnetic saturation 69.5 emu/g and 71.4 emu/g [8]. One of the reports on hydrothermal synthesis of CoFe_2O_4 have a reasonable coercivity of 1389.5 G, and the other has coercivity ranges from 1301 to 1410 G before calcination and 1488 to 1799 G after calcination [16]. Cu-doped CoFe_2O_4 prepared by chemical precipitation method showed coercivity ranging from 787.29 G to 34.679 G with Cu doping from 0 to 100% [17]. Cu-doped CoFe_2O_4 by double-sintering ceramic technique reported a maximum coercivity of 284.07 G [7]. The room temperature (300 K) and low temperature (20 K) The study of magnetic properties of nanocrystalline $\text{Cu}_{0.4}\text{Co}_{0.6}\text{Fe}_2\text{O}_4$ prepared by sol–gel auto-combustion method was reported to be 1184.45 Oe and 5689.76 Oe [18]. The literature review found that the reported magnetic coercivity and squareness ratio of Cu-doped CoFe_2O_4 at room temperature is comparably less, and none of the reports gives the complete structural information, including electron density distribution analysis [19]. Hence in the present work, Cu-doped CoFe_2O_4 with composition $\text{Cu}_x\text{Co}_{1-x}\text{Fe}_2\text{O}_4$: $x=0.05, 0.1, 0.15, 0.2$ was synthesized by self-combustion method and some physical

properties, including magnetic properties, were analyzed in one phase. In the next phase the complete structural information and electron density distribution, hence bonding was extracted using precise XRD data.

2 Materials and methods

In the present study, one-step auto-combustion synthesis of Cu-doped CoFe_2O_4 ($\text{Cu}_x\text{Co}_{1-x}\text{Fe}_2\text{O}_4$: $x=0.05, 0.10, 0.15, 0.20$) was adopted. The starting materials used were Copper (II) nitrate hexa hydrate ($\text{Cu}(\text{NO}_3)_2 \cdot 6\text{H}_2\text{O}$), Cobalt (II) nitrate hexa hydrate ($\text{Co}(\text{NO}_3)_2 \cdot 6\text{H}_2\text{O}$), Iron (III) nitrate nonahydrate ($\text{Fe}(\text{NO}_3)_3 \cdot 9\text{H}_2\text{O}$) and amino acetic acid, Glycine ($\text{CH}_2\text{NH}_2\text{COOH}$), without further purification purchased from Alfa Aesar, India. Glycine was used as fuel for the combustion process with fuel–nitrate molar ratio of 2.2 [20].

2.1 Synthesis

In a typical sample synthesis with $x=0.05$ composition, 0.1875 g of $\text{Cu}(\text{NO}_3)_2 \cdot 6\text{H}_2\text{O}$ and 5.529 g of $\text{Co}(\text{NO}_3)_2 \cdot 6\text{H}_2\text{O}$ were dissolved in 15 ml of deionized water. Then, 16.16 g of $\text{Fe}(\text{NO}_3)_3 \cdot 9\text{H}_2\text{O}$ was dissolved in another 15 ml of deionized water. The two solutions were mixed slowly and stirred well using a magnetic stirrer. After proper mixing, at 80 °C, 10 g of glycine was added and stirred well till a gel was formed. Auto-combustion occurs once the gel reaches the combustion temperature, resulting in a fluffy powder releasing a massive volume of gases. As synthesized powder was ground well using a mortar and pestle and then calcinated to 800 °C for two hours in the air. A video clipping of the final stage of the auto-combustion process of sample preparation of the composition $x=0.05$ is given in the following link <https://bit.ly/3HJz68r>.

2.2 Experimental methods

The experimental analysis of the calcinated samples of all the compositions was done after grinding using mortar and pestle. The well ground samples were sieved using 400 mesh (nylon) for powder XRD analysis, scanning electron microscopy (SEM) and energy dispersive X-ray analysis (EDX), UV–Visible spectroscopy and vibration sample magnetometer (VSM) analysis. Rigaku 600D powder X-ray diffraction instrument was used for recording the XRD data with scan range 2θ from 10° to 100°, scan speed 8° per minute and step width 0.02° using Copper target of wavelength

$\lambda_{k\alpha} = 1.54056 \text{ \AA}$. The sample's surface morphology and composition were analyzed and identified using SEM and EDX instrument QUANTA 200F and TESCAN VEGA3 SPH, respectively. The sample constituents' absorption of UV and visible light, thereby the optical band gap, was analyzed by UV–Visible spectrophotometer, instrument-JASCO V-630, with a wavelength range from 2000 \AA to 8000 \AA . VSM instrument, Lakeshore 7410S was used for the analysis of the magnetization inside the sample with a maximum applied magnetic field of 1.5 T.

2.3 Computational techniques

2.3.1 Rietveld refinement method

The powder XRD profile fitting was done using least square refinement (Rietveld) [21] utilizing JANA2006 software [22]. The initially assumed structure is cubic spinel structure with space group $Fd-3m$. The occupation of the ions in various sites is represented as tetrahedral A site in (0, 0, 0) and octahedral B site in (0.625, 0.625, 0.625) and oxygen ion position (0.375, 0.375, 0.375) position with cell parameter ($a = b = c = 8.40 \text{ \AA}$). The Rietveld analysis using least square approach is adopted for a perfect fit of theoretical line profile with the experimental data profile. The parameters were suitably refined manually until the difference between theoretical model and experimental XRD data reduces to a minimum possible weighted profile reliability index value. Some of the major parameters used for the present refinement are background using Legendre polynomials, unit cell dimensions ($a, b, c, \alpha, \beta, \gamma$), peak width parameters (u, v, w), multiple peak shape parameters (Pseudo-Voight), asymmetry by Berar Baldinozzi, scale factors, preferred orientation by March Dollase, roughness by Bragg–Brentano geometry, atomic positional parameters and their site occupancy (a_i), atomic displacement parameters (ADP), etc. The average structural information and structure factor corresponding to each Bragg peaks were calculated.

2.3.2 Charge density analysis

One of the best mathematical tools for calculating electronic structure is the Maximum Entropy Method. The real and imaginary parts of the structural information obtained from Rietveld refinements were used for MEM calculations. Initially, the unit cell of the crystal is partitioned into $(128 \times 128 \times 128)$ voxels. The entropy maximization calculation in each voxel was calculated, which can then be converted into the charge on each voxel. The software Dynomia [23] was used for MEM computations employing entropy maximization with suitable Lagrangian parameter λ and a minimum number of iterations for the convergence factor $C = 1$. The three-dimensional and two-dimensional

electron density visualization graph in each voxel of the unit cell was plotted using the graphical program VESTA [24]. The numerical one-dimensional electron density between bonding ions was calculated and correlated with the results obtained from 3 and 2D visualization.

3 Results and discussion

3.1 Experimental results

3.1.1 X-ray diffraction methods

Figure 1 is a plot of raw X-ray intensity profile for all the prepared compositions of the sample with 2θ scan range from 10° to 100° with step size 0.02° along with JCPDS data for CoFe_2O_4 . All the observed significant peaks corresponding to (hkl) planes confirm the formation of the single-phase cubic spinel ferrite with space group $Fd-3m$, without any impurity [25, 26]. The enlarged diagram of the raw XRD peaks of the (hkl) planes (113), (400) and (440), is given in inset of Fig. 1, which shows a slight 2θ left shift as the concentration of Cu^{2+} doping is increased. The lattice parameter and cell volume based on unit cell [27] refinement from Table. 1 has a slight increase in value from $8.3986(2) \text{ \AA}$ to $8.4098(2) \text{ \AA}$ and 592.418 \AA^3 to 594.781 \AA^3 as the doping concentration increases from $x = 0.05$ to $x = 0.20$. The above result arises due to the difference in the ionic radius of dopant ion (ionic radius of $\text{Cu}^{2+} = 0.73 \text{ \AA}$) and host ions, both Co^{2+} and Fe^{3+} (ionic radius of Co^{2+} and $\text{Fe}^{3+} = 0.72, 0.63 \text{ \AA}$) occupying octahedral B site as per the XRD data-based cation distribution analysis.

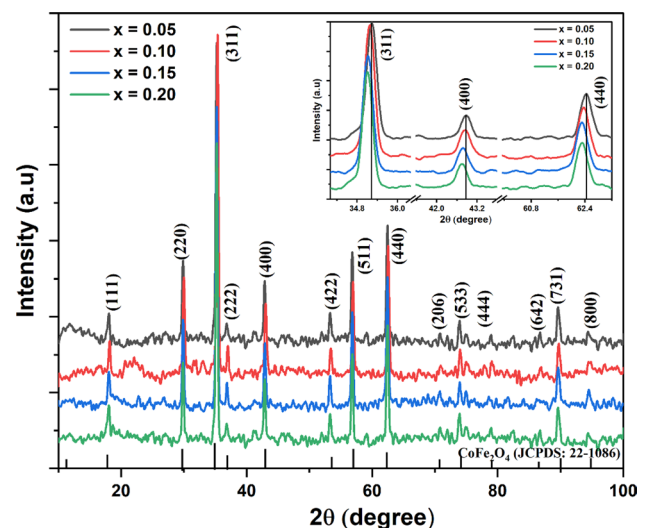
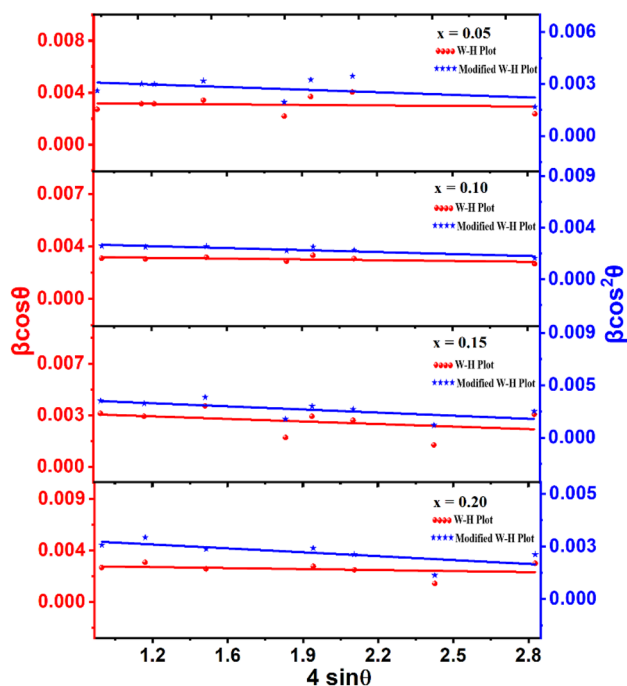


Fig. 1 Raw X-ray intensity profile with inset showing peak shift

Table 1 Observed grain size, strain and lattice parameter

Sample Cu _x Co _{1-x} Fe ₂ O ₄	Williamson Hall method		Modified Williamson Hall method		Debye Scherrer method Grain size (nm)	Unit cell refinement Lattice parameter (Å)
	Strain (10 ⁻⁴)	Grain size (nm)	Strain (10 ⁻⁴)	Grain size (nm)		
x=0.05	-1.282	41 ± 0.5	-4.861	38 ± 0.2	46 ± 0.8	8.398(6)
x=0.10	-1.803	43 ± 0.9	-5.313	40 ± 0.1	46 ± 0.1	8.399(5)
x=0.15	-5.286	35 ± 0.2	-9.004	32 ± 0.4	47 ± 0.8	8.408(4)
x=0.20	-2.696	42 ± 0.1	-6.436	38 ± 0.1	53 ± 0.1	8.409(8)

**Fig. 2** Williamson Hall and modified Williamson Hall plot: Grain size and strain analysis

Williamson Hall (W-H) [28] and modified Williamson Hall plot [29] are shown in Fig. 2, which yields crystallite size and micro strain. The graph is drawn between $4\sin\theta$ in x-axis and $\beta\cos\theta$ and $\beta\cos^2\theta$ in the y-axis for the Williamson Hall and modified Williamson Hall plots, respectively. The numerical results of grain size and lattice strain by both W-H and modified W-H methods are given in Table 1. All the sample compositions show a negative and minimal value of strain, which may be due to the minor compressive strain in the lattice due to dopants [30]. The maximum and minimum grain sizes 40 ± 0.1 nm and 32 ± 0.4 nm is observed for the composition $x = 0.1$ and 0.15 , respectively, based on the modified W-H method, which was reported as a reliable one [29]. It is also found that there is no linear relation of crystallite size with doping concentration.

3.1.2 Cation distribution methods

The distribution of Cu^{2+} , Co^{2+} and Fe^{3+} cations among the tetrahedral A and octahedral B sites will be vital in fine-tuning magnetic properties [31]. The cation distribution can also be analyzed using X-ray intensity ratio method, Mossbauer, Rietveld and magnetic analysis [32]. In this study, the Bertaut method [33] using XRD data and Rietveld-based refinement methods were adopted to understand the distribution of cations in different sites for all doping concentrations of the prepared samples. Bertaut method adopts the comparative intensity ratio I_{220}/I_{400} , I_{220}/I_{440} , I_{400}/I_{440} , and I_{400}/I_{422} calculations of the theoretical and experimental cation active Bragg planes (220), (440), and (400), (422) [34]. The possible cation distribution is given below in the following expression (1) based on the theoretical intensity calculation using Eq. (2) [35].

$$\left[\text{Cu}_\alpha^{2+}\text{Co}_\beta^{2+}\text{Fe}_{1-\alpha-\beta}^{3+}\right]^A \left[\text{Cu}_{x-\alpha}^{2+}\text{Co}_{1-x-\beta}^{2+}\text{Fe}_{1+\alpha+\beta}^{3+}\right]^B \text{O}_4^{2-}, \quad (1)$$

$$I_{hkl}^{\text{cal}} = \left|F_{hkl}^{\text{cal}}\right|^2 P_{hkl}^{\text{cal}} L_p, \quad (2)$$

where α and β are the distribution of Cu^{2+} and Co^{2+} in A site with the assumption that the total occupancy of the A site is one and B site is two, respectively, and I_{hkl}^{cal} , F_{hkl}^{cal} , P_{hkl}^{cal} and L_p are the intensity of the lattice plane (hkl), its structure factor, multiplicity factor, and Lorentz polarization factor. Table 2 gives the cation occupancy in A and B sites, which shows the complete occupation of Fe^{3+} ions in the tetrahedral A site. Both Cu^{2+} and Co^{2+} ions occupied in the octahedral B site completely in all compositions of the prepared samples. The exact occupation of cation in A and B site were given by Rietveld refinement method by refining the occupancy (a_i) of each cation in different sites. Preference of Co^{2+} ions occupation in octahedral B site was already reported earlier [36]. Table 4 gives the parameters refined using cation distribution among A and B sites. It is found that radius of tetrahedral A site increases from 0.5514 \AA to 0.577 \AA for the composition $x = 0.05$ – 0.15 and

Table 2 Cation active XRD intensity ratios and cation distribution

Sample composition $\text{Cu}_x\text{Co}_{1-x}\text{Fe}_2\text{O}_4$	Cation distribution							
	I_{220}/I_{400}		I_{400}/I_{440}		XRD intensity method		Rietveld method	
	Cal	Obs	Cal	Obs	Occupancy in tetrahedral A and octahedral B site		Occupancy in tetrahedral A and octahedral B site	
				A site	B site	A site	B site	
$x=0.05$	1.475	1.090	0.801	0.944	$(\text{Fe}_{1.0})^A$	$(\text{Cu}_{0.05}\text{Co}_{0.95}\text{Fe}_{1.0})^B$	$(\text{Fe}_{0.998})^A$	$(\text{Cu}_{0.054}\text{Co}_{0.949}\text{Fe}_{1.006})^B$
$x=0.10$	1.469	1.129	0.802	0.914	$(\text{Fe}_{1.0})^A$	$(\text{Cu}_{0.10}\text{Co}_{0.90}\text{Fe}_{1.0})^B$	$(\text{Fe}_{0.997})^A$	$(\text{Cu}_{0.104}\text{Co}_{0.900}\text{Fe}_{1.001})^B$
$x=0.15$	1.470	1.042	0.808	0.898	$(\text{Fe}_{1.0})^A$	$(\text{Cu}_{0.15}\text{Co}_{0.85}\text{Fe}_{1.0})^B$	$(\text{Fe}_{0.994})^A$	$(\text{Cu}_{0.138}\text{Co}_{0.85}\text{Fe}_{1.012})^B$
$x=0.20$	1.463	1.106	0.807	0.819	$(\text{Fe}_{1.0})^A$	$(\text{Cu}_{0.20}\text{Co}_{0.80}\text{Fe}_{1.0})^B$	$(\text{Fe}_{0.989})^A$	$(\text{Cu}_{0.216}\text{Co}_{0.805}\text{Fe}_{1.007})^B$

then suddenly decreases to 0.4787 Å for the composition $x=0.2$. Similarly, Octahedral B site decreases from 0.7477 Å to 0.7369 Å for the composition $x=0.05-0.15$ and then suddenly increases to 0.7941 Å for the composition $x=0.2$. The hopping length of both tetrahedral A site and octahedral B site increases with increase in doping concentration and A site has greater hopping length than B site as reported [37]. The other parameters like inter atomic distances (Me–Me) and (Me–O) and angles are also given in Table 3.

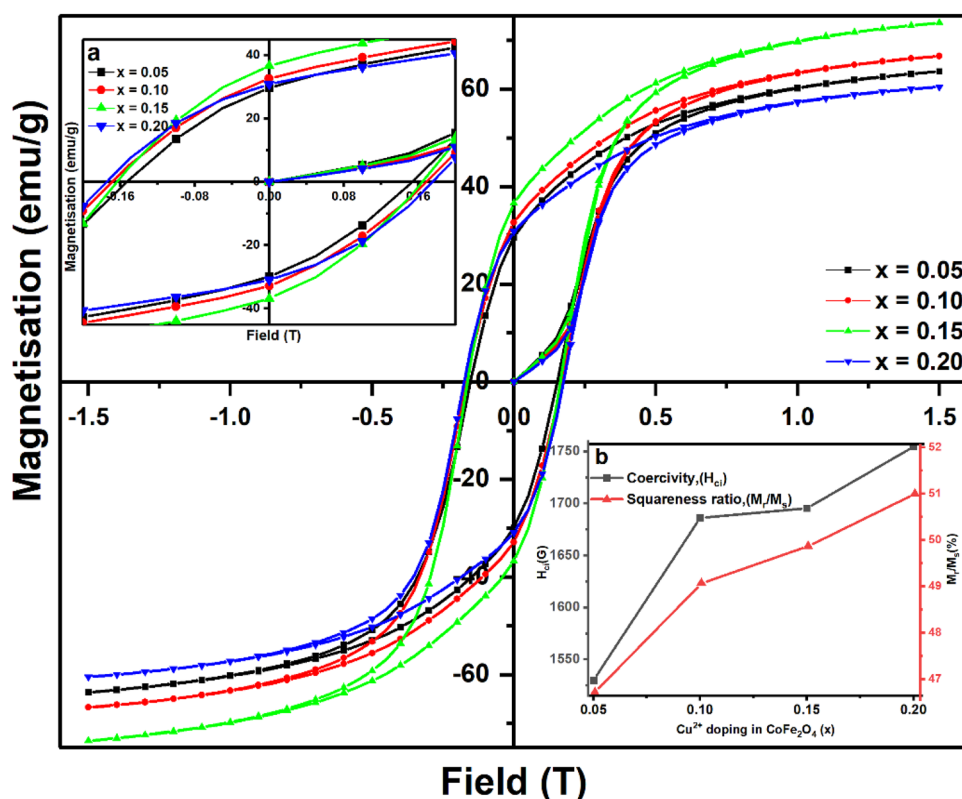
3.1.3 Magnetic hysteresis results

The magnetic properties of all compositions of the doped system were analyzed using VSM measurements, which is shown in Fig. 3. The insets (a) and (b) of Fig. 3 represent the expanded view of the hysteresis for a better understanding of the coercivity and retentivity and the relation of coercivity and squareness ratio (M_r/M_s) with doping concentration, respectively. The maximum observed coercivity and squareness ratio is 1754.67 G and 0.51 for

Table 3 Refined structural parameters based on cation distribution analysis

Calculated parameters		$x=0.05$	$x=0.10$	$x=0.15$	$x=0.20$
Tetrahedral A site (Å)	Radii r_A	0.5514	0.5634	0.5770	0.4787
	Shared edge length d_{AE}	3.0560	3.0756	3.0979	2.9364
	Hopping length L_A	3.6352	3.6359	3.6398	3.6400
Octahedral B site (Å)	Radii r_B	0.7477	0.7414	0.7369	0.7941
	Shared edge length d_{BE}	2.8803	2.8618	2.8459	3.0077
	Unshared edge length d_{BEU}	2.9688	2.9697	2.9732	2.9721
	Hopping length L_B	2.9681	2.9687	2.9719	2.9720
Interatomic distances and angles					
M_e-M_e (Å)	b	2.9681	2.9687	2.9719	2.9720
	c	3.4805	3.4811	3.4849	3.4851
	d	3.6352	3.6359	3.6398	3.6400
	e	5.4529	5.4539	5.4597	5.4600
	f	5.1410	5.1420	5.1475	5.1470
	M_e-O (Å)	p	2.0676	2.0612	2.0561
q		1.8717	1.8838	1.8976	1.7980
r		3.5840	3.6073	3.6337	3.4430
s		3.6533	3.6579	3.6657	3.6321
Angles (°)		θ_1	124°04'	123°48'	123°49'
	θ_2	148°21'	147°08'	147°08'	157°51'
	θ_3	91°44'	92°07'	92°07'	89°19'
	θ_4	125°39'	125°45'	125°45'	125°06'
	θ_5	76°30'	75°47'	75°47'	81°27'

Fig. 3 VSM magnetic hysteresis with inset **a** enlarged version and **b** coercivity and squareness ratio graph



the composition $x = 0.2$ of $\text{Cu}_x\text{Co}_{1-x}\text{Fe}_2\text{O}_4$. The squareness ratio of all the prepared samples is in the range from 0.467 to 0.51 indicating a single domain magnetic structure [38, 39]. The magnetic saturation (M_s) and remanent magnetization (M_r) range from 60.48 to 73.58 emu/g and 29.73 to 36.70 emu/g, in which the maximum value for both parameters are reported for the composition $x = 0.15$. The literature survey reveals so many works reported on the synthesis by various methods and their magnetic hysteresis study of Cu-doped CoFe_2O_4 at room temperature and low temperatures [40]. The maximum coercivity of 1185.45 Oe and 5689.56 Oe at 300 K and 20 K were reported in the article “Dielectric and Magnetic Behavior

of Nanocrystalline $\text{Cu}_{0.4}\text{Co}_{0.6}\text{Fe}_2\text{O}_4$ Ferrite” by sol–gel auto-combustion method [18]. Most authors reported fewer coercivity values even at room temperature and low temperatures [16, 41–43]. This may be the first research article for the Cu-doped CoFe_2O_4 series, reporting a maximum coercivity value of 1754.67 G and a squareness ratio of 51% at room temperature ($\text{Cu}_{0.2}\text{Co}_{0.8}\text{Fe}_2\text{O}_4$) by sol–gel auto-combustion method. Inset (b) of Fig. 3 reveals almost a linear response. The experimental magnetic parameters and theoretical Bohr magneton values are given in Table 4. The experimental Bohr magneton (μ_B^H) was calculated from the magnetization value at 1.5 T using the following relation [44]

Table 4 Experimental and theoretical magnetic hysteresis parameters using VSM

Parameters	Composition			
	$x = 0.05$	$x = 0.10$	$x = 0.15$	$x = 0.20$
Saturation magnetization M_s (emu/g)	63.6448	66.7714	73.5873	60.4813
Remnant magnetization M_r (emu/g)	29.735	32.761	36.704	30.847
Coercivity H_{ci} (G)	1529.86	1686.36	1695.39	1754.67
Squareness ratio	0.467	0.490	0.498	0.51
Observed Bohr magneton μ_B^H	2.953	2.800	3.083	2.532
Calculated Bohr magneton μ_B^N (Neel's)	2.941	2.824	2.778	2.721
Cation distribution based on μ_B^H	$(\text{Co}_{0.013}\text{Fe}_{0.987})^A$ $(\text{Cu}_{0.05}\text{Co}_{0.937}\text{Fe}_{1.013})^B$	$(\text{Fe}_{1.0})^A$ $(\text{Cu}_{0.10}\text{Co}_{0.90}\text{Fe}_{1.0})^B$	$(\text{Co}_{0.095}\text{Fe}_{0.905})^A$ $(\text{Cu}_{0.15}\text{Co}_{0.755}\text{Fe}_{1.095})^B$	$(\text{Fe}_{1.0})^A$ $(\text{Cu}_{0.20}\text{Co}_{0.80}\text{Fe}_{1.0})^B$

$$\mu_B^H = \frac{(\text{Molecular weight of the sample})}{5585} \times M_s. \quad (3)$$

The cation distribution in A and B sites was calculated and reported in Table 4 using the experimental Bohr magnetron value calculated using the Eq. (3). The distribution of cations has a perfect correlation with the values calculated using X-ray intensity methods for the compositions $x=0.1$ and 0.2 . A small contribution of Co^{2+} in tetrahedral A site for the compositions $x=0.05$ and 0.15 is estimated, which contributes a reduction of saturation value. However, the most probable final cation distribution was calculated using the fine Rietveld refinement of the atomic occupancy of A and B site ions and also the anion. The Neel's Bohr magnetron (μ_B^N) is a theoretical value calculated based on the concept of the antiparallel alignment of the down spin and up spin magnetic moment of electrons in tetrahedral A and octahedral B sites, respectively, and the final Rietveld-based cation distribution analysis using the relation $\mu_B^N = M_B - M_A$, in which M_B and M_A are the B site and A site magnetization. The collinearity between experimental and theoretical Bohr magnetron values shows that the grown system almost obeys Neel's two sublattices, the collinear model.

3.1.4 Energy band gap analysis

The energy bandgap of the prepared compositions of the Cu-doped CoFe_2O_4 spinel ferrites was analyzed using the UV-Visible spectrophotometry analysis, utilizing deuterium source for UV part and tungsten source for visible part. The measured range of wavelength of the absorption was from 2000 \AA to 8000 \AA with a step size of 2 \AA . The energy band gap is calculated by plotting energy in eV in the x-axis vs $(\alpha h\nu)^2$ in $\text{eV}^2/\text{cm}^{-2}$. The tangent of the linear part of the curve touching the x-axis by extrapolation gives the energy bandgap values, which is shown in Fig. 4. It is observed that all samples show direct bandgap character with a numerical value ranging from 2.801 eV to 2.950 eV . Typically, the violet color region varies from 380 to 450 nm . The absorption range of all the prepared samples in this work is from 420 to 442 nm . This shows that these samples may be used for selective violet color absorption of very high-frequency applications as well as photocatalytic applications [45].

3.1.5 Surface morphology and composition analysis

Most of the physical properties depend on the size and shape of the particle, mainly in the nano range. Scanning electron microscopy (SEM) is one of the best experimental tools to study the visual morphology of the surface. In the present study, SEM micrograph was taken with scale factor $1 \mu\text{m}$, magnifications 45.2 , 48.7 , 30.8 and 18.2 kX and potential

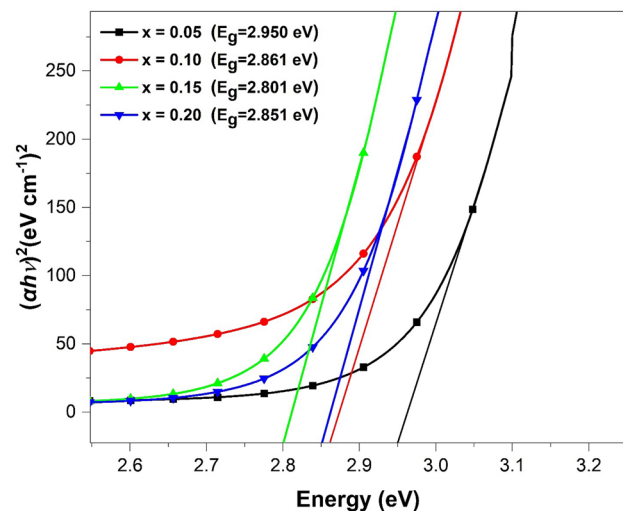


Fig. 4 Energy band gap using UV-Visible absorption spectrum

30 kV for the compositions $x=0.05$ – 0.20 , respectively, given in the inset (a) of Fig. 5. No perfect spherical nature is seen in any of the inset (a) of Fig. 5. The inset (b) of Fig. 5 shows the histogram diagram and Gaussian distribution graph for all compositions of $\text{Cu}_x\text{Co}_{1-x}\text{Fe}_2\text{O}_4$. A highly agglomerated and porous nature is seen from all the SEM images, with the maximum for the composition $x=0.20$. The average particle size using SEM analysis is found to be 90.63 nm , 151.40 nm , 73.81 nm and 348.51 nm , respectively, for the compositions $x=0.05$, 0.1 , 0.15 , 0.2 . As the average particle size of all samples is high above an optimum value, it leads to high magnetic coercivity, specially for the composition $x=0.4$. Also, the particle size is directly related to the scattering efficiency. Energy-dispersive X-ray analysis (EDX) reveals the precise elemental composition of the sample under investigation. Figure 5 gives the EDX-based elemental composition of the all samples. All the EDX images show the elements Cu, Co, Fe, and O without any other impurities.

3.2 Computational results

3.2.1 XRD powder profile analysis

The unit cell's structural information and structure factor corresponding to each Bragg plane was computed adopting the Rietveld methodology using JANA2006. The refined structural information and reliability indices are given in Table 5. It is found from Table 5 that there is an expansion of the unit cell, which is confirmed by the slight increase in lattice parameter and cell volume in correlation with the shift in X-ray intensity peaks towards the lower 2θ angles. There is a slight deviation in the oxygen displacement parameter from the ideal position of 0.375 . The deviation is maximum

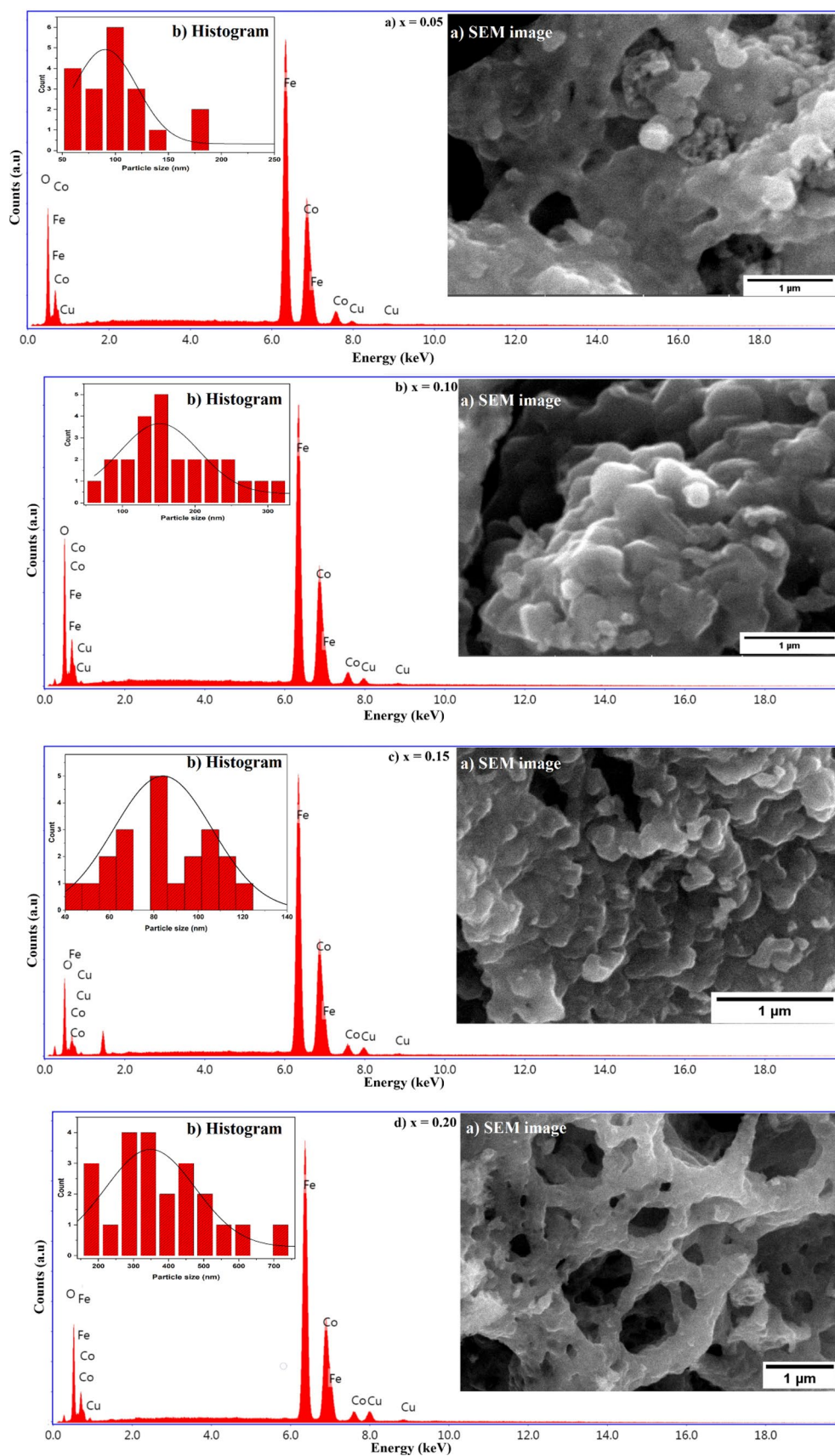


Fig. 5 EDX analysis with inset a the SEM image and inset b the particle size histogram for $\text{Cu}_x\text{Co}_{1-x}\text{Fe}_2\text{O}_4$: a $x = 0.05$, b $x = 0.1$, c $x = 0.15$, d $x = 0.20$

Table 5 Refined structural parameters and reliability indices of computational techniques

Parameters	Values	$x=0.05$	$x=0.10$	$x=0.15$	$x=0.20$
<i>Refined structural parameters</i>					
Lattice parameters (Å)	a	8.3953(1)	8.3969(4)	8.4059(1)	8.4063(8)
Unit cell volume (Å ³)	a^3	591.709	592.048	593.953	594.038
Oxygen displacement parameter	U^{43m}	0.3787(9)	0.3795(0)	0.3803(1)	0.3735(2)
<i>Rietveld parameters</i>					
Reliability index (%)	R_{obs}	4.57	3.16	2.03	3.18
Weighted reliability index (%)	wR_{obs}	3.08	1.72	1.40	2.48
Profile reliability index (%)	R_p	1.01	0.91	0.88	1.10
Weighted profile reliability index (%)	wR_p	1.27	1.14	1.10	1.40
No. of electrons/Unit cell	F_{000}	888.8	889.6	890.4	891.2
<i>MEM parameters</i>					
No. of cycles		2401	2219	2250	2781
Initial density (e/Å ³)	F_{000}/a^3	1.5020	1.5025	1.4991	1.5002
Lagrange parameter	λ	0.022	0.0183	0.0189	0.0321
Reliability index (%)	R_{MEM}	6.85	6.62	7.60	7.77
Weighted reliability index (%)	wR_{MEM}	3.92	3.76	3.62	3.86

for the composition $x=0.15$ [46]. All the Rietveld reliability factors are minimal for all compositions with a slight acceptable error, showing the perfectness of the refinement process based on the crystallographic model of cubic spinel ferrite with space group $Fd-3m$.

The JANA2006 fitted profile and experimental XRD intensity data in arbitrary units are shown in Fig. 6 for reference for the composition $x=0.05$. The JANA2006 profile

for the other compositions is given in the supplementary file, named "Supplementary Fig. 1. Figure 6 perfectly visualizes the refinement of all the experimentally observed Bragg planes with the model-based profile with the inset showing the expanded form of Bragg peaks (113) and (404) in which the perfect matching of experimental and observed data points are seen. The supplementary table named "Supplementary Table 1" presents the observed and calculated

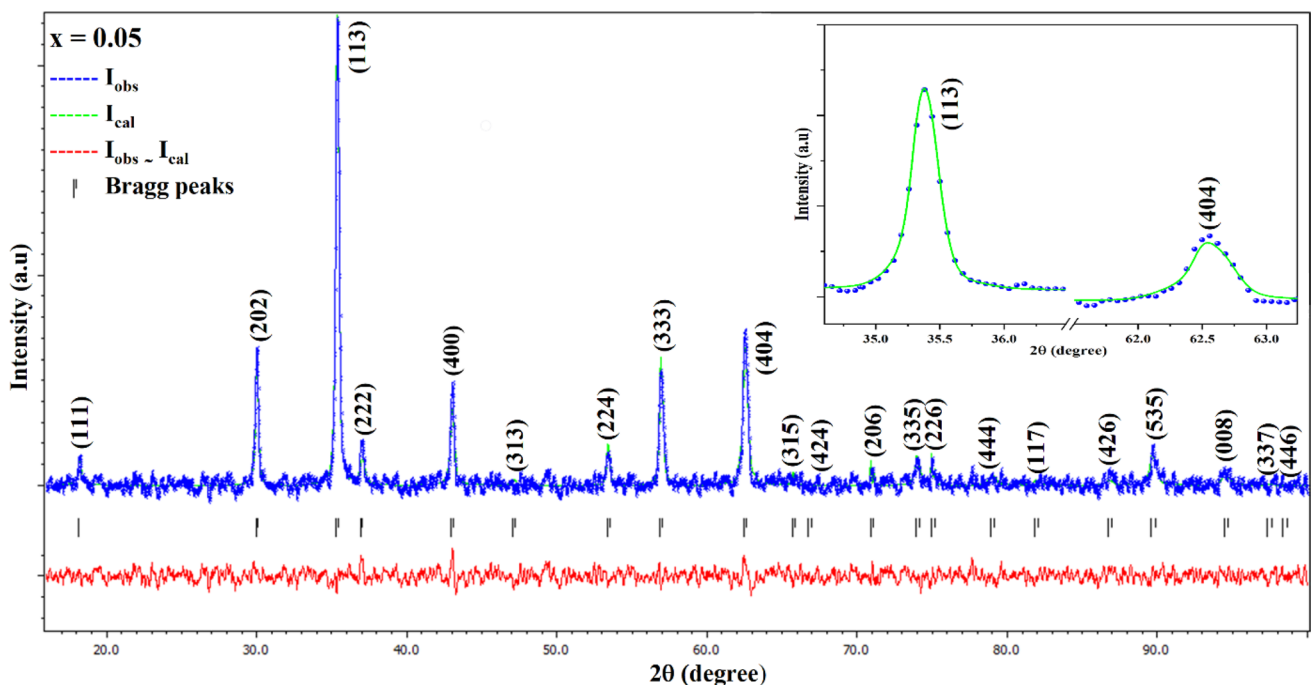


Fig. 6 Fitted JANA2006 profile for the composition $x=0.05$ with inset its expanded form showing fine fitting of observed and calculated intensity

structure factor for various principal Bragg planes for all compositions of the prepared samples, in which the difference between the two is minimal.

3.2.2 Electron charge analysis

The success of electron density analysis based on MEM has been proved by the successful explanation of the electronic structure of different application-oriented materials by many researchers [41, 47–49]. The accurate electron density distribution without error due to series termination is possible with the minimum number of structure factors. In this work, the real and imaginary parts of the structure factor for all lattice planes from the diffraction angle 10° to 100° were calculated and used as the input for the MEM calculations. The initial electron density per voxel is fixed as F_{000}/a^3 . The electron density at each voxel was calculated by entropy maximization by fixing the proper Lagrangian parameter λ for the minimum number of iterations. 3D visual mapping using VESTA for the prepared composition $x=0.2$ with iso-surface level $0.45 \text{ e}/\text{\AA}^3$ for half of the unit cell (for better clarity) is given in Fig. 7. The presence of tetrahedral A and octahedral B sites in alternating octants confirms the formation of cubic spinel structure with the electron cloud around each ion, giving the complete visualization of the shape, distribution of electrons, type and strength of bonding. A solid covalent bonding in tetrahedral A site and moderate ionic bonding in octahedral B site was revealed from Fig. 7. A moderately localized spherical charge distribution is seen in the octahedral B site.

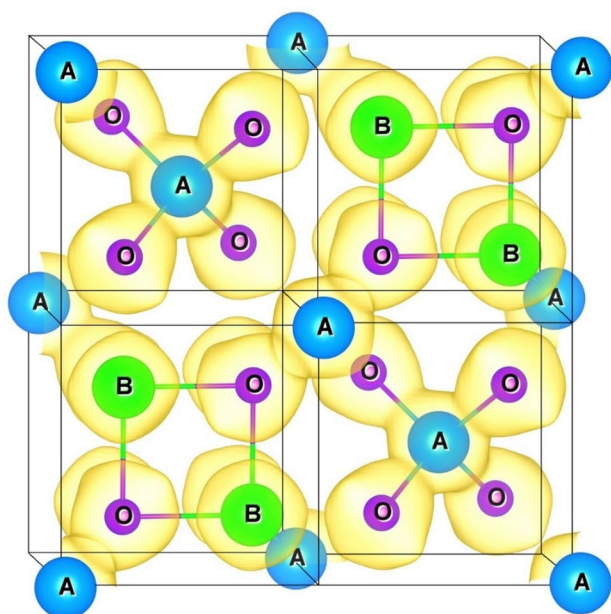


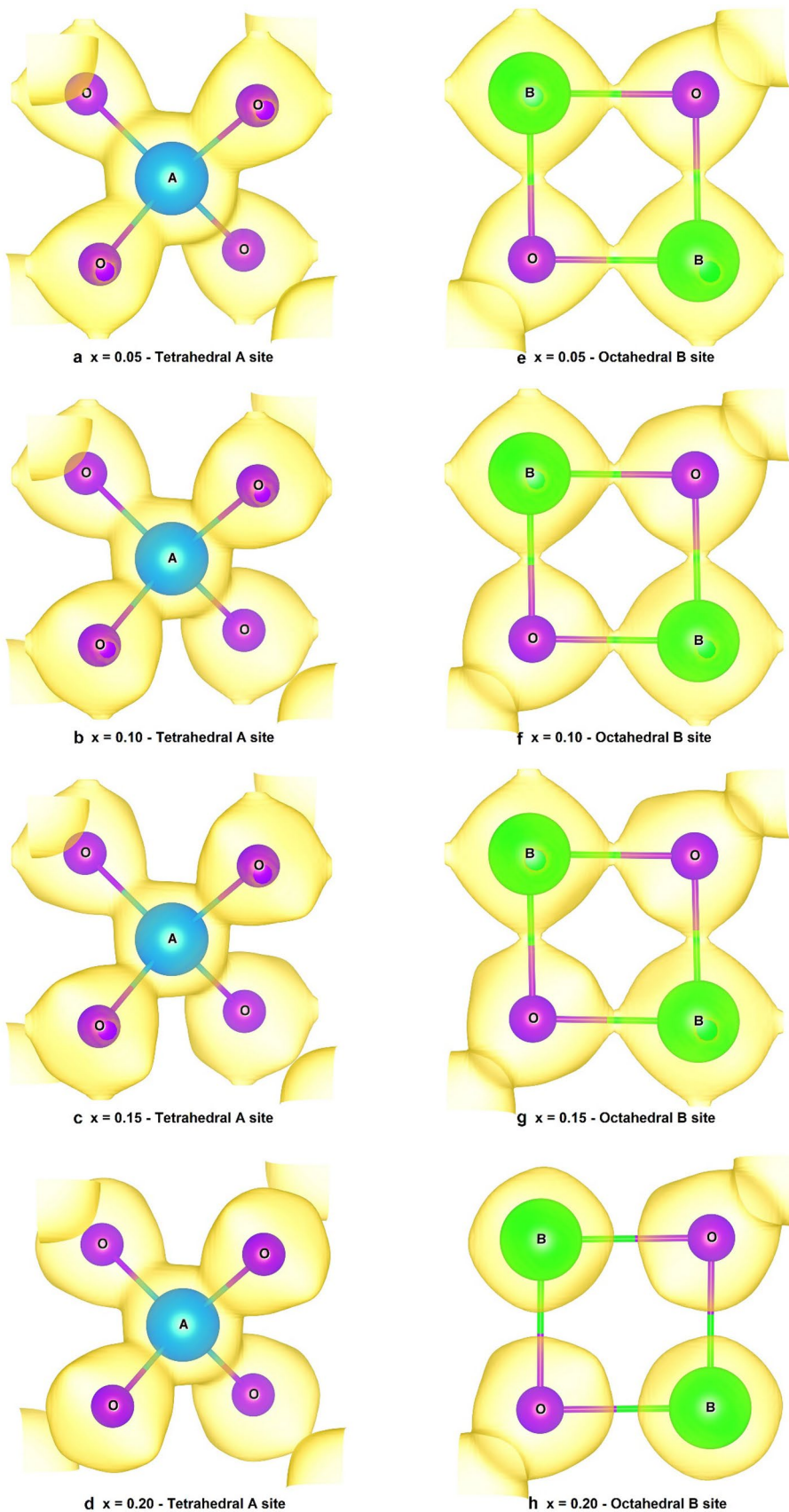
Fig. 7 3D MEM electron density in half unit cell of the composition $x=0.20$ with iso-surface level $0.45 \text{ e}/\text{\AA}^3$

The visual three-dimensional electron density variation in the half unit cell with boundary $x=0.5-1$ and $y, z=0-1$ is given in Fig. 8 (a–h) in the same iso-surface level ($0.45 \text{ e}/\text{\AA}^3$) for comparison for all the compositions. As revealed by Fig. 8(a–d), tetrahedral A site bonding in all compositions was highly covalent with maximum sharing of electrons between A and O ions in all compositions and maximum for the composition $x=0.05$ and minimum for the composition $x=0.15$. In the octahedral B site, mild B–O covalent bonding and complete ionic bonding are seen in Fig. 8 (e–h) for the compositions $x=0.05-0.15$ and $x=0.2$.

The electron density distribution along the plane (110) with contour level ($0-1 \text{ e}/\text{\AA}^3$) with interval $0.08 \text{ e}/\text{\AA}^3$ is plotted in Fig. 9 for the compositions $x=0.05-0.2$. The numerical value of the mid bond density at the A–O and B–O bonding regions is also given in Fig. 9(a–d). Among the super exchange interactions, A–A, A–B and B–B, A–B is the strongest, A–A is the weakest, and B–B is moderate for all compositions as reported earlier for spinel ferrites [34]. There is one exception in A–A bonding for the composition $x=0.05$, which has higher A–A interaction may be due to the charge enhancement by the neighboring ions. Overall, A–O interaction is strong covalent and B–O interaction mild covalent/ionic in all compositions $x=0.05-0.2$. It is empirically found that the spinel ferrite material with maximum A–O covalent and B–O ionic bonding behave as a ferromagnetic material with maximum coercivity.

One-dimensional electron density profile between various interacting sites and the numerical mid bond distance and electron density as inset table are shown in Fig. 10 (a–f). Figure 10a gives the A–A super exchange electron interaction for all compositions showing the increasing mid bond distance with doping concentration and minimum mid bond density except for the sample $x=0.05$, which has the numerical bond value $0.371 \text{ e}/\text{\AA}^3$. Figure 10b gives the A–B super exchange charge interaction for all compositions showing the increasing mid bond distance from 2.1718 \AA to 2.2443 \AA with doping concentration with almost constant numerical mid bond density nearly $0.2 \text{ e}/\text{\AA}^3$. Figure 10c gives the B–B super exchange charge interaction for all compositions showing the increasing mid bond distance from 1.4841 \AA to 1.4860 \AA with increasing doping concentration with an almost constant numerical mid bond density of nearly $0.12 \text{ e}/\text{\AA}^3$. The mid bond density A–B is maximum, A–A is minimum, and B–B is moderate, except for the sample $x=0.05$, in which A–A has the maximum bonding. Figure 10d gives the A–O charge interaction for all compositions showing the decreasing mid bond distance from 0.9589 \AA to 0.9131 \AA with random variation in mid bond density and minimum for the composition $x=0.15$. Figure 10e gives the B–O charge interaction for all compositions showing almost a constant mid bond distance with the minimum, mid bond density

Fig. 8 a–h 3D electron density with iso-surface $0.45 e/\text{\AA}^3$ showing Tetrahedral A and Octahedral B sites



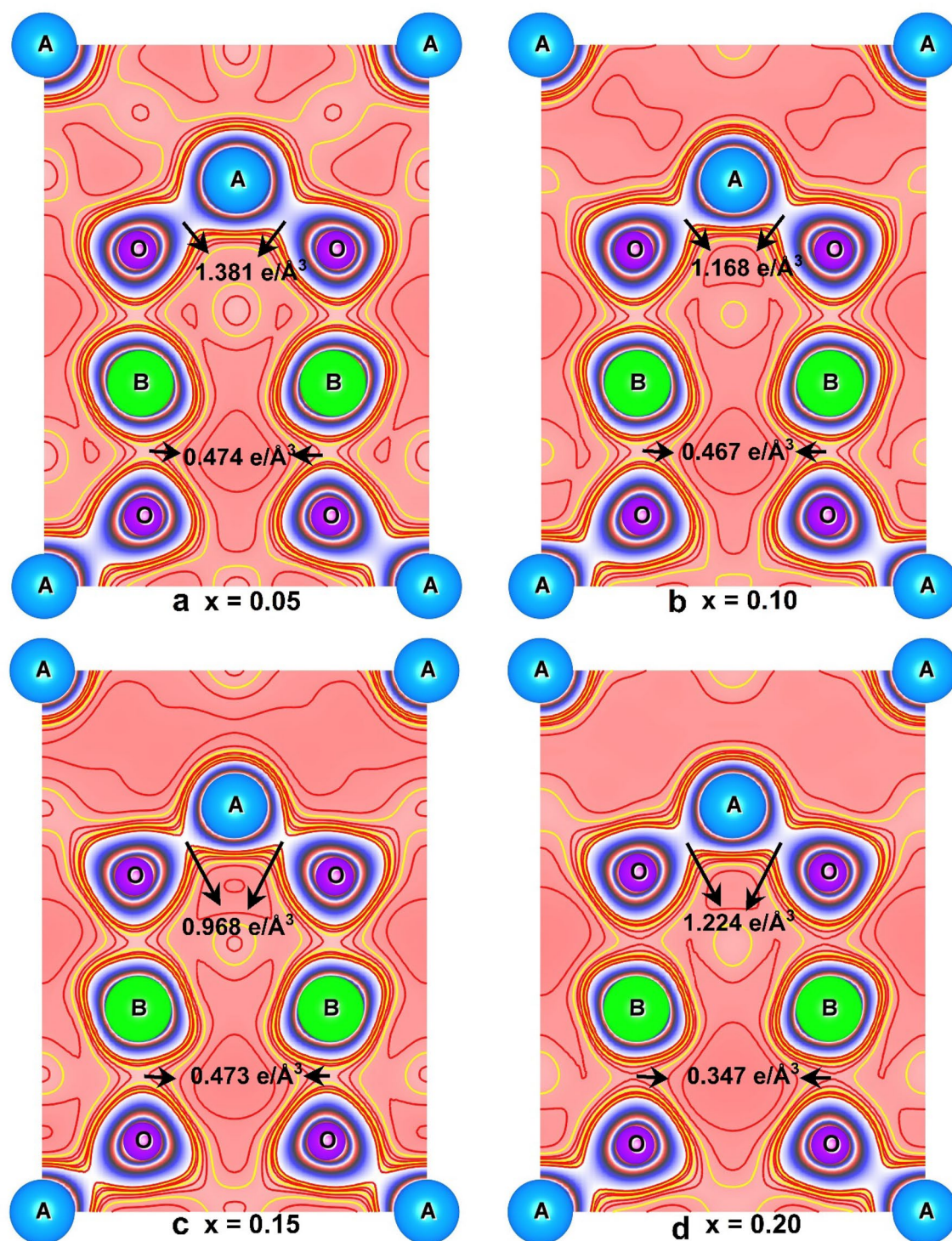


Fig. 9 2D electron density along (1 1 0) lattice plane with contour level (0–1 $\text{e}/\text{\AA}^3$) and interval $0.08 \text{ e}/\text{\AA}^3$

for the composition $x = 0.20$, which may be a requirement for better coercivity. O–O mid bond interaction density

is almost a constant in all compositions (Fig. 10f), nearly $0.12 \text{ e}/\text{\AA}^3$ and minimum for the composition $x = 0.20$.

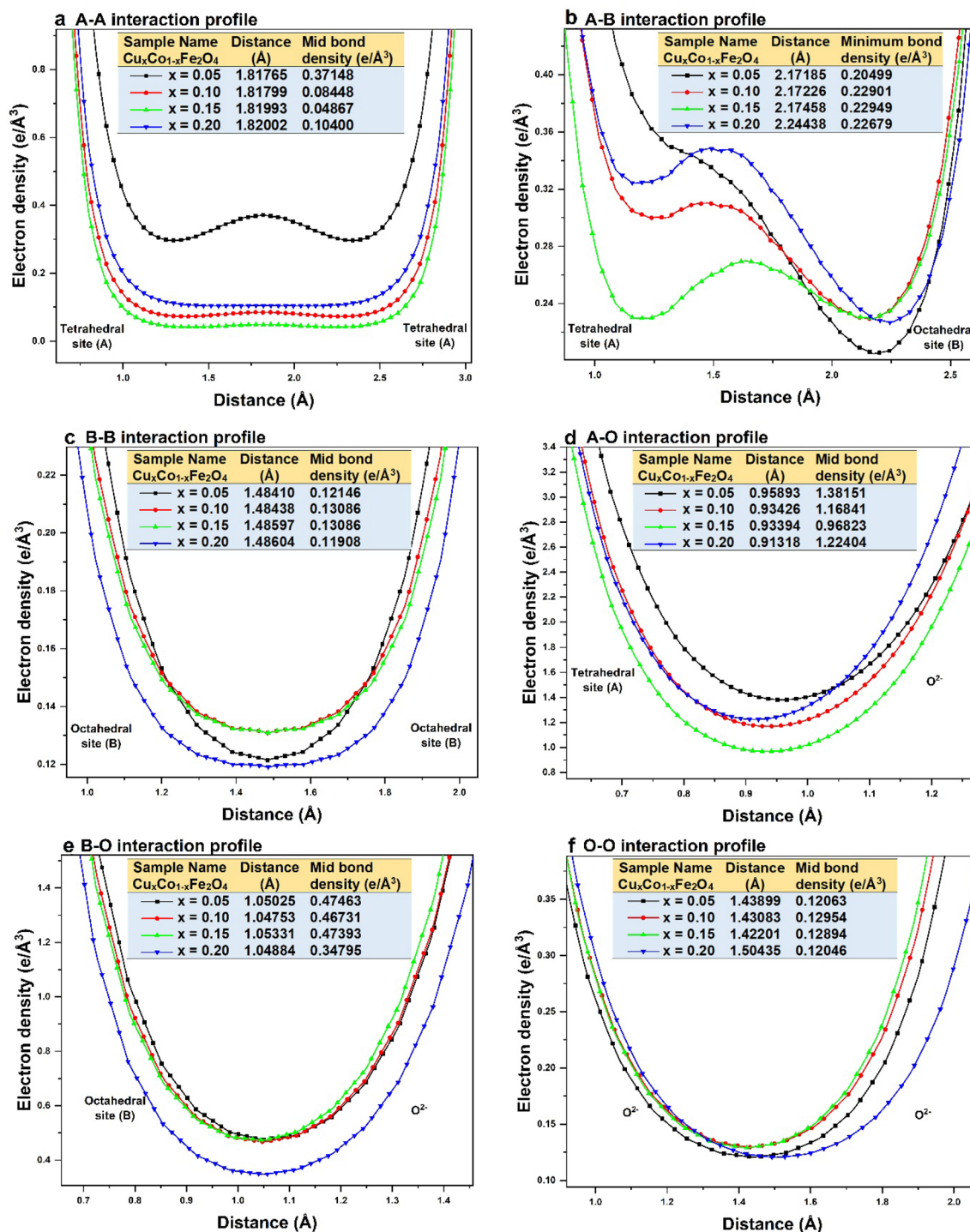


Fig.10 One-dimensional electron density profile with a A–A, b A–B, c B–B, d A–O, e B–O and f O–O interaction

4 Conclusion

Phase pure cubic spinel structure of Cu²⁺-doped CoFe₂O₄ (Cu_xCo_{1-x}Fe₂O₄; x = 0.05, 0.1, 0.15, 0.2) was successfully synthesized by a single step simple self-combustion method using glycine as fuel under atmospheric conditions.

Powder X-ray diffraction intensity-based peak shift and lattice parameter show a minor expansion of the unit cell with increased doping of Cu²⁺ in CoFe₂O₄. Cation distribution analysis confirms inverse spinel ferrite structure. All samples show minimal compressive lattice strain and average crystallite size ranges from 32 ± 0.4 nm and 40 ± 0.1 nm for the

composition $x=0.15$ and $x=0.10$, respectively, based on the modified Williamson Hall method. The magnetic hysteresis analysis show variation of coercivity (H_{ci}) and squareness ratio (M_r/M_s) from 1529.86 G to 1754.67 G and 0.46–0.51, respectively, almost following a linear increase with doping. The observed maximum coercivity and squareness ratios are 1754.67 G and 0.51 for the sample $\text{Cu}_{0.2}\text{Co}_{0.8}\text{Fe}_2\text{O}_4$. The above result may be the maximum coercivity and squareness ratio reported at room temperature for Cu-doped CoFe_2O_4 spinel systems to the best of our knowledge. The experimental and theoretical Bohr magneton values almost coincide, showing that the grown system perfectly obeys Neel's two sublattices, the collinear model. MEM electron density distribution reveals complete electronic structure and bonding. It can be empirically confirmed that the composition of spinel ferrite material with maximum A–O covalent and B–O ionic bonding behave as a ferromagnetic material with maximum coercivity. The prepared composition $\text{Cu}_{0.2}\text{Co}_{0.8}\text{Fe}_2\text{O}_4$ may be a better alternative for semi hard ferrite applications. High optical absorption in the violet region of the visible spectrum can make the sample a good photocatalytic material. Further through investigation of the sample may lead the material, a magnetic recording and/or magnetic drug delivery applications.

Supplementary Information The online version contains supplementary material available at <https://doi.org/10.1007/s00339-022-05808-2>.

Acknowledgements The authors acknowledge the Basic Scientific Research Instrumentation Centre, Jayaraj Annappaikam College for women, Periyakulam for powder XRD data and SAIF, Indian Institute of Technology, Madras (IITM) for VSM measurements. Instrumental Facilities, CIC, Madurai Kamaraj University for SEM and EDX, Department of Chemistry, Hajee Karutha Rowther Howdia College, Uthamapalayam for UV–Visible spectrophotometry studies. The authors sincerely thank Principal and management, Hajee Karutha Rowther Howdia College, Uthamapalayam 625 533, Tamil Nadu, for their constant support and encouragement to the research activities.

CRedit author statement M. Thavarani: Investigation, writing original draft. M. Charles Robert: Supervision, Conceptualization, Methodology. N. Pavithra: Executing graphical techniques, Resources, S. Balaji Prasath: Data Curation, writing review and editing, Y.B. Kannan: Formal analysis and validation, A. Ansar Ahamed: Electronic artwork and editing.

Funding This research did not receive specific grant from any funding agencies.

Data availability The authors declare that all the experimental data are deposited and publicly available in Mendeley data repository link <http://doi.org/10.17632/hj9spgpcjn.1>

Declarations

Conflict of interest The authors declare that they have no known direct or indirect financial interests or non-financial relationship that could have influence this reported work.


References

1. M. Faraji, Y. Yamini, M. Rezaee, J. Iran. Chem. Soc. **717**, 1 (2010)
2. J. Rivas, M. Bañobre-López, Y. Piñero-Redondo, B. Rivas, M.A. López-Quintela, J. Magn. Mater. **324**, 3499 (2012)
3. D. D. Stueber, J. Villanova, I. Aponte, Z. Xiao, and V. L. Colvin, *Pharmaceutics* **13**, (2021).
4. P. Yang, J. Sun, X. Zhang, P. Shang, *Kexue Tongbao/Chinese. Sci. Bull.* **64**, 741 (2019)
5. F.G. da Silva, J. Depeyrot, A.F.C. Campos, R. Aquino, D. Fiorani, D. Peddis, *J. Nanosci. Nanotechnol.* **19**, 4888 (2019)
6. S. Amiri, H. Shokrollahi, *Mater. Sci. Eng. C* **33**, 1 (2013)
7. M.A. Ahmed, S.F. Mansour, M.A. Abdo, *Phys. Scr.* **84**, 055602 (2011)
8. A.S. Ponce, E.F. Chagas, R.J. Prado, C.H.M. Fernandes, A.J. Terzeo, E. Baggio-Saitovitch, *J. Magn. Mater.* **344**, 182 (2013)
9. Z. Zi, Y. Sun, X. Zhu, Z. Yang, J. Dai, W. Song, *J. Magn. Mater.* **321**, 1251 (2009)
10. Z. Wang, X. Liu, M. Lv, P. Chai, Y. Liu, X. Zhou, J. Meng, *J. Phys. Chem. C* **112**, 15171 (2008)
11. A. Kalam, A.G. Al-Sehemi, M. Assiri, G. Du, T. Ahmad, I. Ahmad, M. Pannipara, *Results Phys.* **8**, 1046 (2018)
12. I. Sharifi, H. Shokrollahi, M.M. Doroodmand, R. Safi, *J. Magn. Mater.* **324**, 1854 (2012)
13. R.S. Yadav, I. Kuřitka, J. Vilcakova, J. Havlica, L. Kalina, P. Urbánek, M. Machovsky, D. Skoda, M. Masař, M. Holek, *Ultrason. Sonochem.* **40**, 773 (2018)
14. K. Kombaiah, J.J. Vijaya, L.J. Kennedy, M. Bououdina, R.J. Ramalingam, H.A. Al-Lohedan, *Mater. Chem. Phys.* **204**, 410 (2018)
15. C. Cannas, A. Musinu, D. Peddis, G. Piccaluga, *Chem. Mater.* **18**, 3835 (2006)
16. S. Moosavi, S. Zakaria, C.H. Chia, S. Gan, N.A. Azahari, H. Kaco, *Ceram. Int.* **43**, 7889 (2017)
17. M. Margabandhu, S. Senthilnathan, S. Senthilkumar, D. Gajalakshmi, *Brazilian Arch. Biol. Technol.* **59**, 16161046 (2017)
18. P. Jadoun, J. Sharma, B.L. Prashant, S.N. Dolia, D. Bhatnagar, V.K. Saxena, *A.I.P. Conf. Proc.* **1731**, 050065 (2016)
19. K.V. Siva, A. Kumar, A. Arockiarajan, *J. Magn. Mater.* **535**, 168065 (2021)
20. A.B. Salunkhe, V.M. Khot, M.R. Phadatare, S.H. Pawar, *J. Alloys Compd.* **514**, 91 (2012)
21. H.M. Rietveld, *J. Appl. Cryst.* **2**, 65 (1969)
22. V. Petříček, M. Dušek, and L. Palatinus, *Zeitschrift Fur Krist. – Cryst. Mater.* **229**, 345 (2014).
23. K. Momma, T. Ikeda, A.A. Belik, F. Izumi, *Powder Diffr.* **28**, 184 (2013)
24. K. Momma, F. Izumi, *J. Appl. Crystallogr.* **41**, 653 (2008)
25. S.R. Naik, A.V. Salker, S.M. Yusuf, S.S. Meena, *J. Alloys Compd.* **566**, 54 (2013)
26. K. Pubby, S. S. Meena, S. M. Yusuf, and S. Bindra Narang, *J. Magn. Mater.* **466**, 430 (2018).
27. T.J.B. Holland, S.A.T. Redfern, *Mineral. Mag.* **61**, 65 (1997)
28. G.K. Williamson, W.H. Hall, *Acta Metall.* **1**, 22 (1953)
29. P.M. Kibasomba, S. Dhlamini, M. Maaza, C.P. Liu, M.M. Rashad, D.A. Rayan, B.W. Mwakikunga, *Results Phys.* **9**, 628 (2018)
30. H.S. Kim, N.G. Park, *NPG Asia Mater.* **12**, 1 (2020)
31. J. Hua, Z. Cheng, Z. Chen, H. Dong, P. Li, and J. Wang, (2021).
32. M.A. Amer, M. El Hiti, *J. Magn. Mater.* **234**, 118 (2001)
33. D.S. Nikam, S.V. Jadhav, V.M. Khot, R.A. Bohara, C.K. Hong, S.S. Mali, S.H. Pawar, *RSC Adv.* **5**, 2338 (2015)
34. V.K. Lakhani, T.K. Pathak, N.H. Vasoya, K.B. Modi, *Solid State Sci.* **13**, 539 (2011)
35. S.M. Patange, S.E. Shirsath, S.S. Jadhav, K.M. Jadhav, *Phys. Status Solidi Appl. Mater. Sci.* **209**, 347 (2012)

36. M. N. Akhtar, N. Yahya, and P. Bin Hussain, *Int. J. Basic Appl. Sci.* **09**, 37 (2009).
37. D.D. Andhare, S.A. Jadhav, M.V. Khedkar, S.B. Somvanshi, S.D. More, K.M. Jadhav, *J. Phys. Conf. Ser.* **1644**, 012014 (2020)
38. A.R. Kagdi, N.P. Solanki, F.E. Carvalho, S.S. Meena, P. Bhatt, R.C. Pullar, R.B. Jotania, *J. Alloys Compd.* **741**, 377 (2018)
39. H.N. Chaudhari, P.N. Dhruv, C. Singh, S.S. Meena, S. Kavita, R.B. Jotania, *J. Mater. Sci. Mater. Electron.* **31**, 18445 (2020)
40. M. A. Almessiere, Y. Slimani, A. D. Korkmaz, N. Taskhandi, M. Sertkol, A. Baykal, S. E. Shirsath, Ercan, and B. Ozçelik, *Ultrason. Sonochem.* **58**, 104621 (2019).
41. R. Ade, S.S. Kumar, S. Valanarasu, S.S. Kumar, S. Sasikumar, V. Ganesh, Y. Bitla, H. Algarni, I.S. Yahia, *Ceram. Int.* **47**, 24031 (2021)
42. P. Chitra, E.R. Kumar, T. Pushpagiri, A. Steephen, *J. Supercond. Nov. Magn.* **34**, 1239 (2021)
43. D. Gupta, V. Rishi, and T. K. Gupta, <https://doi.org/10.1080/14328917.2020.1831145> **25**, 393 (2020).
44. C. Choodamani, G. P. Nagabhushana, S. Ashoka, B. Daruka Prasad, B. Rudraswamy, and G. T. Chandrappa, *J. Alloys Compd.* **578**, 103 (2013).
45. E. Casbeer, V.K. Sharma, X.Z. Li, *Sep. Purif. Technol.* **87**, 1 (2012)
46. R.S. Yadav, I. Kuřitka, J. Vilcakova, J. Havlica, J. Masilko, L. Kalina, J. Tkacz, J. Švec, V. Enev, M. Hajdúchová, *Adv. Nat. Sci. Nanosci. Nanotechnol.* **8**, 045002 (2017)
47. S. Saravanakumar, D. Sivaganesh, V. Sivakumar, S. Sasikumar, T.K. Thirumalaisamy, M.A. Sayed, A.M. Ali, *Phys. Scr.* **96**, 125817 (2021)
48. D. Sivaganesh, S. Saravanakumar, V. Sivakumar, S. Sasikumar, J. Nandha Gopal, S. Kalpana, and R. Rajajeyaganthan, *J. Mater. Sci. Mater. Electron.* **31**, 8865 (2020).
49. M.C. Robert, M. Thavarani, N. Pavithra, S.B. Prasath, R. Saravanan, Y.B. Kannan, *J. Supercond. Nov. Magn.* **2022**, 1 (2022)

Publisher's Note Springer Nature remains neutral with regard to jurisdictional claims in published maps and institutional affiliations.

Authors and Affiliations

M. Thavarani¹ · M. Charles Robert²  · N. Pavithra¹ · S. Balaji Prasath² · Y. B. Kannan³ · A. Ansar Ahamed²

✉ M. Charles Robert
jothycharles@gmail.com

¹ Department of Physics, Sri Adi Chunchanagiri Women's College, Cumbum, Tamil Nadu, India

² Research Centre and PG Department of Physics, Hajee Karutha Rowther Howdia College, Uthamapalayam, Tamil Nadu, India

³ Department of Physics, Arumugam Pillai Seethai Ammal College, Tiruppattur, Tamil Nadu, India